INTERNATIONAL JOURNAL FOR NUMERICAL AND ANALYTICAL METHODS IN GEOMECHANICS
Int. J. Numer. Anal. Meth. Geomech. 2000; **00**:1–6 *Prepared using* nagauth.cls *[Version: 2002/09/18 v1.02]*

Smooth particle hydrodynamics simulations of low Reynolds number flows through porous media†

David W. Holmes[1,*,‡], John R. Williams[2,§] and Peter Tilke[3,¶]

[1] *Civil and Environmental Engineering, Massachusetts Institute of Technology, 77 Massachusetts Avenue, Cambridge, MA 02139-4307*
[2] *Civil and Environmental Engineering and Engineering Systems, Massachusetts Institute of Technology, 77 Massachusetts Avenue, Cambridge, MA 02139-4307*
[3] *Department of Mathematics and Modeling, Schlumberger-Doll Research Center, 1 Hampshire Street, Cambridge, MA 02139-1578*

SUMMARY

In this paper, a three-dimensional smooth particle hydrodynamics (SPH) simulator for modeling grain scale fluid flow in porous media is presented. The versatility of the SPH method has driven its use in increasingly complex areas of flow analysis, including, the characterization of flow through permeable rock for both groundwater and petroleum reservoir research. SPH provides the means to model complex multi-phase flows through such media however acceptance of the methodology has been hampered by the apparent lack of actual verification within the literature, particulary in the three-dimensional case. In this paper, the accuracy of SPH is addressed via a comparison to the previously recognized benchmarks of authors such as Sangani and Acrivos (1982), Zick and Homsy (1982) and Larson and Higdon (1989) for the well defined classical problems of flow through idealized two- and three-dimensional porous media. The accuracy of results for such low Reynolds number flows is highly dependent on the implementation of no-slip boundary conditions. A new, robust, and numerically efficient, method for implementing such boundaries in SPH is presented. Simulation results for friction coefficient and permeability are shown to agree well with the available benchmarks. Copyright © 2000 John Wiley & Sons, Ltd.

KEY WORDS: Smooth Particle Hydrodynamics; No-Slip Boundary Conditions; Friction Coefficient; Permeability; Consolidated Porous Media

---

*Correspondence to: D. W. Holmes, Civil and Environmental Engineering, Massachusetts Institute of Technology, 77 Massachusetts Avenue, Cambridge, Massachusetts 02139-4307 USA. Tel.: (617)452-3395; e-mail: dholmes@mit.edu.
†Work presented in part at the 10th U.S. National Congress on Computational Mechanics
‡Postdoctoral Fellow
§Professor of Information Engineering
¶Scientific Advisor

Contract/grant sponsor: Schlumberger-Doll Research Center; Saudi Aramco

1. INTRODUCTION

Understanding the behavior of fluids as they flow through permeable rock is important to a variety of contemporary problems in earth science and engineering. Oil recovery, groundwater contamination and carbon sequestration represent a few such areas where improved understanding of pore scale flow may result in significant enhancements. A variety of existing numerical techniques are capable of simulating porous media to determine important properties such as permeability, relative permeability, capillary pressure, etc (eg. Stokes solvers [1, 2, 3, 4], finite difference [5, 6, 7], finite element [6, 8], lattice-Boltzmann [9], volume of fluid [10], level-sets [11]). Few of these methods, however, have been demonstrated to accurately simulate the complex 3D multi-phase immiscible and miscible fluid behaviors characteristic of problems in geological flow. For problems where the physics at the grain scale is dominated by phenomena such as surface tension and wettability, simulating the effect rather than the cause can limit the insight which can be achieved. Smooth particle hydrodynamics (SPH) is one of the few numerical methods capable of realistically modeling actual phase interactions, however, the little amount of verification work published on the method has hindered its acceptance.

SPH is a mesh-free Lagrangian particle method first proposed for astrophysical problems by Lucy [12] and Gingold and Monaghan [13] and now widely applied to fluid mechanics problems [14, 15, 16, 17, 18, 19] and continuum problems involving large deformation [19, 20] or brittle fracture [21]. A key advantage of particle methods such as SPH (see also dissipative particle dynamics (DPD) [22, 23]) is in their ability to advect mass with each particle, thus removing the need to explicitly track phase interfaces for problems involving multiple fluid phases or free surface flows. There is a computational price for managing free particles, however, in many circumstances this expense can be justified by the versatility with which a variety of multi-physics phenomena can be included. Additionally, new parallel hardware architectures such as multi-core [24] are removing many of the barriers which have traditionally limited the practicality of high resolution numerical techniques like SPH.

While the ability to simulate a diverse range of complex phenomena with SPH represents a key advantage over alternate methods, the accuracy of such a method must be supported by verifying tests on more simple, single-phase benchmark problems. The performance of SPH in the reproduction of one-dimensional flow characteristics have been well defined in the literature (Takeda et al [25], Morris et al [26], Sigalotti et al [27]). Additionally, two-dimensional flows past systems such as periodic arrays of cylinders (Morris et al [26], Zhu et al [16], Zhu and Fox [28]) and more complex flow obstructions (Zhu and Fox [28]) have demonstrated good agreement with conventional numerical and analytical solutions to the same problems. For the case of three-dimensional flow, however, verification of SPH remains largely untreated within the published literature. Ordered sphere packs are an idealized three-dimensional porous media and modeling flow through such media has commonly been used as a standard test problem to verify the three-dimensional accuracy of a numerical method [1, 2, 3, 4]. Simulating such a system using SPH will go a long way towards verifying the method and validating its more advanced capabilities.

In what follows, we first present some of the fundamentals of the exact form of SPH used in this work. The development of a new method for enforcing no-slip boundary conditions in SPH is then detailed. Following this, results are presented for flow simulations of several well defined one-, two- and three dimensional flow problems as a means to verify both the new no-slip boundary method, and the SPH method itself. It will be shown that the results

demonstrate excellent agreement with previously published benchmarks.

2. SMOOTH PARTICLE HYDRODYNAMICS

Comprehensive reviews of smooth particle hydrodynamics theory have been published by various authors including Benz [29], Monaghan [14, 17] and Liu and Liu [19]. In what follows we provide a brief overview of the fundamentals of the specific form of SPH used in this work and its implementation[†]. This is followed by the development of a new methodology for no-slip boundary conditions for use in low Reynolds number flow simulations.

2.1. Fundamentals

In SPH, a fluid volume is discretized it into a set of disordered 'integration points' or 'particles'. Those particles then advect with the fluid velocity in a Lagrangian sense. SPH field approximations for quantities such as density, velocity, etc develop from the exact integral interpolant of a field

$$A(\boldsymbol{r}) = \int A(\boldsymbol{r}')\,\delta(\boldsymbol{r}-\boldsymbol{r}')\,d\boldsymbol{r}' \tag{1}$$

where $A(\boldsymbol{r})$ is a field quantity determined at the position vector $\boldsymbol{r}$, while δ is the Dirac delta function.

Equation (1) defines a value at some specific location, $\boldsymbol{r}$, as being a singularity on a known continuous field. Equation (1) can be approximated by

$$A(\boldsymbol{r}) = \int A(\boldsymbol{r}')\,W(\boldsymbol{r}-\boldsymbol{r}',h)\,d\boldsymbol{r}' \tag{2}$$

where $W(\boldsymbol{r}-\boldsymbol{r}',h)$ is referred to as an *interpolation kernel* or *smoothing function* and now $A(\boldsymbol{r})$ is determined through a weighted interpolation of surrounding field values. This weighting is characterized by the *smoothing length*, h, and should decay with distance from $\boldsymbol{r}$.

For consistency, the kernel W typically approximates a Gaussian satisfying the conditions

$$\int W(\boldsymbol{r}-\boldsymbol{r}',h)\,d\boldsymbol{r}' = 1 \tag{3}$$

and

$$\lim_{h\to 0} W(\boldsymbol{r}-\boldsymbol{r}',h) = \delta(\boldsymbol{r}-\boldsymbol{r}') \tag{4}$$

Due to the nature of a Gaussian function, the contribution of field values outside of some finite support domain tend toward zero. For numerical efficiency it is convenient to impose a *compact support* on the smoothing function where only values within some specified bound

$$W(\boldsymbol{r}-\boldsymbol{r}',h) = 0 \quad \text{when} \quad |\boldsymbol{r}-\boldsymbol{r}'| > \kappa h \tag{5}$$

are considered to have non-negligible effect, see Fig. 1. The parameter κ is chosen to ensure that an adequate proportion of the function resides in each support domain to ensure the error associated with such an assumption is small.

[†]The reader is referred to the aforementioned works for a more definitive overview.

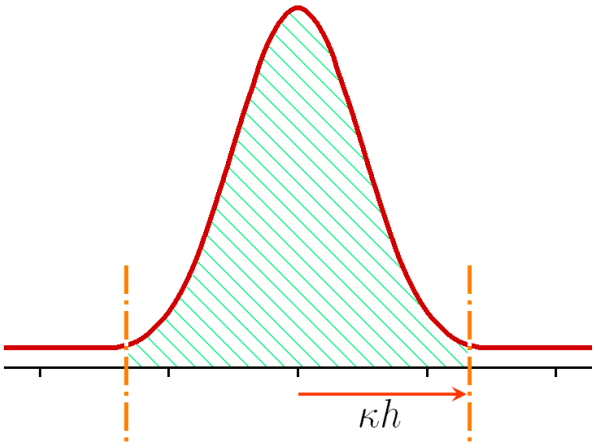

Figure 1. The compact support imposed on an otherwise infinite Gaussian support domain.

By discretizing the fluid volume into a finite number of disordered integration points or 'particles', (2) can be approximated by the summation interpolant

$$A_i = \sum_j \frac{m_j}{\rho_j} A_j W\left(\boldsymbol{r}_i - \boldsymbol{r}_j, h\right) \tag{6}$$

where smoothing length h is generally set as the initial particle spacing, m_j and ρ_j are the mass and density of particle j at position $\boldsymbol{r}_j$, and the fraction m_j/ρ_j accounts for the approximate volume of space each particle represents to maintain consistency between the continuous (2) and the discrete (6) forms of the field expression. Correspondingly, the gradient of A is given

$$\nabla A_i = \sum_j \frac{m_j}{\rho_j} A_j \nabla_i W\left(\boldsymbol{r}_i - \boldsymbol{r}_j, h\right) \tag{7}$$

Fig. 2 illustrates a smoothing function for a single integration point in space, a.

Authors such as Tartakovsky and Meakin [30, 18] and Hu and Adams[31] have suggested a variation to (6) and (7) where a *particle number density* term, n_i is used in place of ρ_i/m_i where

$$n_i = \frac{\rho_i}{m_i} \tag{8}$$

and now

$$A_i = \sum_j \frac{A_j}{n_j} W\left(\boldsymbol{r}_i - \boldsymbol{r}_j, h\right) \tag{9}$$

$$\nabla A_i = \sum_j \frac{A_j}{n_j} \nabla_i W\left(\boldsymbol{r}_i - \boldsymbol{r}_j, h\right) \tag{10}$$

Applying (9) to the particle number density itself, n_i can be given in terms of the smoothing function as

$$n_i = \sum_j W\left(\boldsymbol{r}_i - \boldsymbol{r}_j, h\right) \tag{11}$$

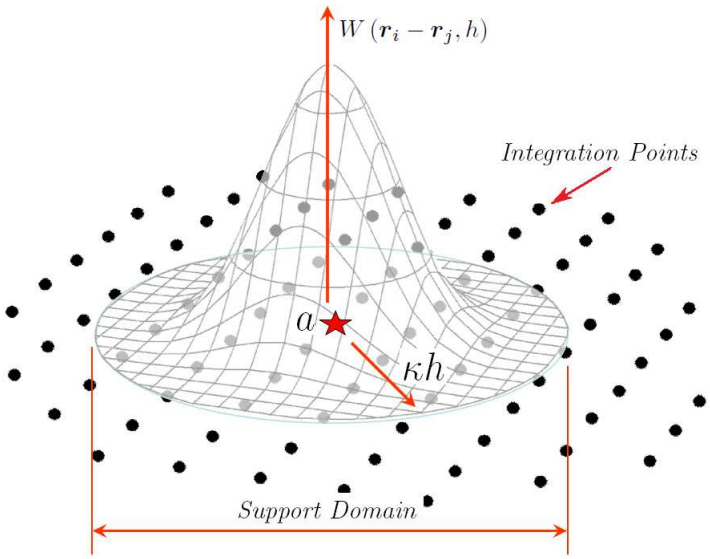

Figure 2. The support domain and smoothing function in 2D for some particle a.

and similarly, mass density of each particle can be given

$$\begin{aligned}\rho_i &= m_i n_i \\ &= m_i \sum_j W(\boldsymbol{r}_i - \boldsymbol{r}_j, h)\end{aligned} \tag{12}$$

This expression conserves mass exactly, much like the summation density approach of conventional SPH [19].

Use of a particle number density variant of the SPH formulation is typically motivated by the need to accommodate multiple fluid phases of significantly differing densities [30, 18, 31]. Use of (9) and (10) eliminates the artificial surface tension effects observed by Hoover [32] and removes density discrepancies which would otherwise manifest at phase interfaces. In this paper consideration of multi-phase flow has been left to future publication, however, the particle number density formulation has been retained because of other advantages which will become apparent later in Section 2.2.

Determination of particle velocity is achieved through discretization of the Navier-Stokes conservation of linear momentum equation. In this work, a modified version of the expression provided by Morris et al [26] and used by Tartakovsky and Meakin [30] has been used, where

$$\begin{aligned}\frac{dv_i^\alpha}{dt} = &-\frac{1}{m_i}\sum_{j=1}^{N}\left(\frac{P_i}{n_i^2}+\frac{P_j}{n_j^2}\right)\frac{\partial W_{ij}}{\partial r_i^\alpha} \\ &+\frac{1}{m_i}\sum_{j=1}^{N}\frac{(\mu_i+\mu_j)}{n_i n_j}\left(v_i^\alpha - v_j^\alpha\right)\frac{r_i^\beta - r_j^\beta}{\left|r_i^\beta - r_j^\beta\right|^2}\cdot\frac{\partial W_{ij}}{\partial r_i^\beta} + F_i^\alpha\end{aligned} \tag{13}$$

where P_i is the pressure, μ_i is the dynamic viscosity, $\boldsymbol{v}_i$ is the particle velocity and $\boldsymbol{F}_i$ is the body force applied on the i^{th} particle. Indices α and β refer to vector components and, β corresponds to an Einstein's summation on the right of the expression.

An equation of state proposed by Morris and co-workers [26, 33, 34] has been used to determine particle pressure at each time step via

$$P_i = c^2 \left(\rho_i - \rho_0\right) \tag{14}$$

where ρ_0 is the fluid reference density while c is the artificial sound speed. Following Morris et al [26], the artificial sound speed term, c, should be chosen according to

$$c^2 \simeq \text{Max}\left(\frac{\rho_0 V_0^2}{\Delta\rho}, \frac{\rho_0 \nu V_0}{L_0 \Delta\rho}, \frac{\rho_0 \left|\boldsymbol{F}\right| L_0}{\Delta\rho}\right) \tag{15}$$

where ν is the kinematic viscosity ($\nu = \mu/\rho_0$), V_0 and L_0 are the velocity and length scales and $|\boldsymbol{F}|$ is the magnitude of body force per unit mass. $\Delta\rho$ is the maximum allowed amount of density fluctuation (generally chosen as being around 1%) meaning that c will scale with the degree of incompressibility of the system.

In this work, we integrate the differential rate equation (13) using a conventional *Leapfrog* [35] numerical integration scheme. A stable solution can be achieved by enforcing the following conditions on the time step length [19, 16, 36]

$$\Delta t \leq 0.125 \frac{h^2}{\nu} \tag{16a}$$

$$\Delta t \leq 0.25 \frac{h}{3c} \tag{16b}$$

$$\Delta t \leq 0.25 \min_i \left(h/3 \left|\boldsymbol{F}_i\right|\right)^{1/2} \tag{16c}$$

Here, $|\boldsymbol{F}_i|$ is the magnitude of force on a particle.

A quintic spline kernel function has been used following Morris [26, 37] such that, given $R = |\boldsymbol{r}_i - \boldsymbol{r}_j|/h$, then

$$W\left(R,h\right) = \alpha_d \times \begin{cases} \left(3-R\right)^5 - 6\left(2-R\right)^5 + 15\left(1-R\right)^5 & 0 \leq R < 1 \\ \left(3-R\right)^5 - 6\left(2-R\right)^5 & 1 \leq R < 2 \\ \left(3-R\right)^5 & 2 \leq R < 3 \\ 0 & 3 \leq R \end{cases} \tag{17}$$

where $\alpha_d = 120/h$, $\alpha_d = 7/(478\pi h^2)$, $\alpha_d = 3/(359\pi h^3)$ in 1, 2 and 3 dimensions respectively.

2.2. Boundary Treatment

Typically, for the permeable rock applications of most interest in this research, fluid flow will occur in the range of low Reynolds numbers. In such circumstances, a no-slip condition exists at solid boundaries and must be enforced within a simulation to achieve accurate flow profiles. Libersky et al [38] first suggested the use of ghost particles for representing SPH boundaries. Such particles are a reflection of real particles through the boundary and an approximation to no-slip conditions can be achieved by designating the ghost particle velocities as being inverse to that of the corresponding real particle. A method developed by Takeda et al [25],

and later used by Sigalotti et al [27], applies a similar theory whereby the velocities of a zone of imaginary boundary particles are determined as a scaled inverse of that of their real counterparts. The relative distances between imaginary and real particles and the boundary are used to determine this scaling. Making further improvements to the method of Takeda et al, Morris et al [26], and later Zhu et al [16], presented what has perhaps become the unofficial standard in SPH no-slip boundary methods. Their method was shown to be highly accurate, particularly for low Reynolds number flows. Later work by Tartakovsky and co workers [18, 36, 39] cited the artificial velocity method of Morris et al as being superior in accuracy to alternative methods, but computationally expensive and, instead, opted for a simpler bounce-back boundary condition.

The computational expense of the method of Morris et al [26] stems from the need to determine a tangent to the boundary surface for each fluid particle[‡]. This requires that either the exact boundary surface be known, or some alternative surface recognition procedure be carried out (such as has been used by Morris in the determination of surface tension effects [34]). Superficial boundary particle velocities are then determined from

$$\boldsymbol{v}_B = -\frac{d_B}{d_A}\boldsymbol{v}_A \tag{18}$$

where d_A and d_B are the normal distances from the tangent to particle A and boundary particle B respectively. Generally d_A is limited to avoid overly large boundary velocities by a condition such as $d_A = \max(d_A, \sqrt{3}h/4)$ [16]. For the general case of complex 3D and/or deformable pore geometries, it is computationally unrealistic to maintain actual boundary surfaces and, as such, complex calculations are necessary to establish boundary tangents dynamically.

It is at this point where the use of the particle number density variant of SPH proves to be a particular advantage. To eliminate the need to determine boundary tangents, we introduce a *state specific particle number density*, $\bar{n}_i$, where

$$\bar{n}_{i,\phi} = \sum_j \delta_{\phi\theta} W\left(\boldsymbol{r}_{i,\phi} - \boldsymbol{r}_{j,\theta}, h\right) \tag{19}$$

and where ϕ and θ indicate the state of respective particles (i.e. fluid or boundary). $\delta_{\phi\theta}$ is the Kronecker delta where

$$\delta_{\phi\theta} = \begin{cases} 1 & \phi = \theta \\ 0 & \phi \neq \theta \end{cases} \tag{20}$$

From (19) and (20) it is evident that only kernel values corresponding to particles of the same sate as particle i will contribute to $\bar{n}_i$. By comparing this state specific particle number density, $\bar{n}_i$, with the actual particle number density, n_i (equation (11)), i.e.

$$\chi_i = \frac{\bar{n}_i}{n_i} \tag{21}$$

the result is a ratio representing the proximity of a particle (fluid or boundary) to the boundary

[‡]Or boundary particles in the case of concave boundaries.

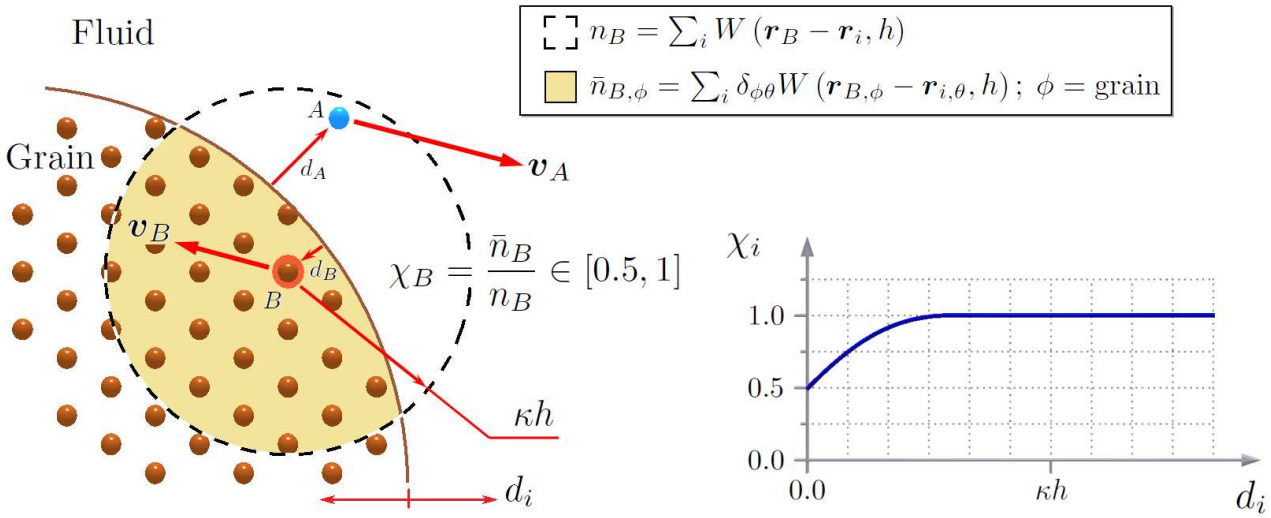

Figure 3. Relationship between proximity ratio and particle distance from the boundary surface.

surface. For the ideal case of a straight boundary, then

$$\chi_i = \begin{cases} 0.5 & d_i = 0 \\ \in (0.5, 1) & 0 < d_i < \kappa h \\ 1 & d_i \geq \kappa h \end{cases} \tag{22}$$

where d_i is the distance of particle i from the boundary surface, see Fig. 3.

Based on (22), it is possible to derive a relationship between fluid and boundary proximity ratios, χ_i, which produces approximately the same degree of velocity scaling as the relationship of Morris et al (equation (18)), i.e.

$$\boldsymbol{v}_B = -\frac{\frac{\kappa h}{0.5}(\chi_B - 0.5)}{\max\left(\frac{\kappa h}{0.5}(\chi_A - 0.5), \frac{\sqrt{3}}{4}h\right)} \boldsymbol{v}_A \tag{23}$$

where, as with equation (18), the denominator is limited to avoid overly large boundary velocities. Also, as per Morris et al, if the boundary has actual motion, $\boldsymbol{v}_A$ in equation (23) should be replaced with the fluid velocity relative to the boundary, i.e. $\boldsymbol{v}_A - \boldsymbol{v}_B$.

While (23) was derived using straight boundaries, in practice we have found that actual proximity ratios of fluid and boundary surface particles will exceed 0.5 for all but the most sharp of boundaries (i.e. angles sharper than $\sim 90°$). This is primarily a result of the significant self contribution of each particle to its own particle number density. As such, equation (23) will enforce a no-slip boundary condition successfully for all boundary profiles, including concave and convex curved boundaries. This is of particular benefit for the case of non-uniform or rough boundaries as might be encountered within permeable rock. If severely sharp boundaries must be accommodated within a model, the numerator of (23) can be limited to $\max(\frac{\kappa h}{0.5}(\chi_B - 0.5), 0)$

to maintain consistency[§].

As a result of the dependance of particle number density on the nonlinear smoothing function, the boundary proximity ratio, χ_i, will only loosely approximate the linear equivalent from the expression of Morris et al (see Fig. 3). Additionally, where Morris et al scaled velocity as a function of normal distance to a tangent, in our approach we scale velocity as a function of distance from the actual boundary interface. In this way, (23) is only approximately equivalent to (18). The advantage of using such a modified artificial velocity method is, however, clear. Provided the particle number density variant of SPH is used, there is almost no additional computational expense associated with enforcing no-slip boundary conditions using the new method. While not an exact reproduction of the boundary behavior of Morris et al, results are presented in later Sections which demonstrate the new method to produce high levels of accuracy thus validating its use.

2.3. Parallel Implementation

While there is a significant amount of published work on pore scale fluid flow using SPH (see for example [30, 18, 16, 39, 33, 28]), there is comparably little on the three-dimensional case. This can almost exclusively be attributed to the significant increase in computational expense associated with extending a complex model to 3D. The SPH code developed in this work has been implemented within a new multi-core simulation framework (the development of which has been presented elsewhere, see [24]), to make three-dimensional simulation viable. Using the *H-Dispatch* programming model developed in [24], scaling results in excess of 70% on a 24-core Dell Server PER900 with Intel Xeon CPU, E7450 @ 2.40 GHz, running 64-bit Windows Server Enterprise 2007, have been achieved. This has made possible the 3D simulation results which will be presented in what follows.

3. TESTING AND VERIFICATION

As a means to verify the accuracy of the developed SPH code, simulations of several well defined one-, two- and three-dimensional flow problems were carried out. Results from these simulations are presented in what follows

3.1. One-Dimensional Flow Problems

Simulations involving one-dimensional flow between infinite plates have typically been used as an initial test of the performance of no-slip boundary conditions in SPH (see for example Morris et al [26], Takeda et al [25], Sigalotti et al [27]). In such conditions, it is possible to develop analytical solutions to the Navier-Stokes equations, thus providing a useful means of comparison.

Following Morris et al [26], we have developed SPH results for both Poiseuille and Couette flow. In both cases, a 2D section of the system was simulated with the plates positioned at $y = 0$ and $y = 10^{-3}m$. $13,668$ particles were initially arranged on a hexagonal grid with

[§]Note, however, that in such circumstances, the physical meaning of both no-slip boundary interactions and, indeed, the SPH formulation itself, may be lost.

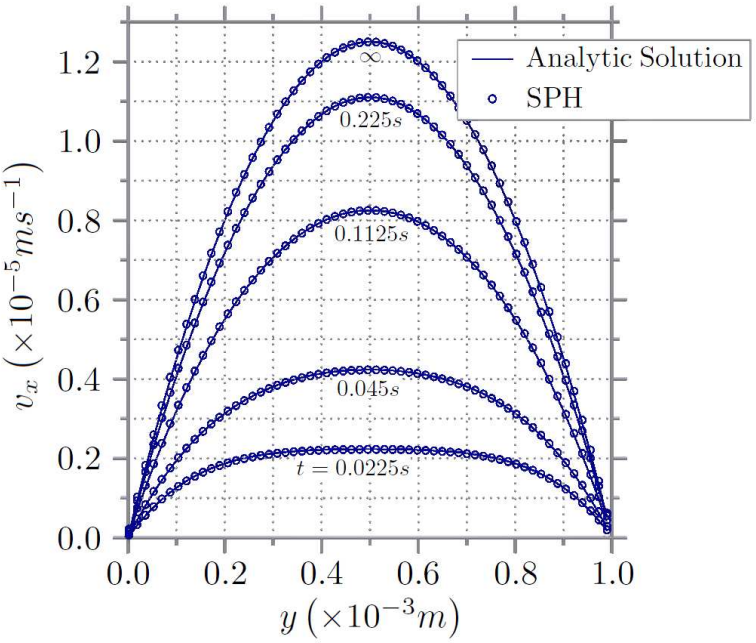

Figure 4. Results for fluid velocity for Poiseuille flow comparing SPH simulation results with the analytical solution.

spacing $h = 2 \times 10^{-5} m$ (see Fig. 6 (a)) and the fluid was assigned the properties of water ($\rho_0 = 10^3 kgm^{-3}$, $\nu = 10^{-6} m^2 s^{-1}$). Periodic boundaries constrained the problem in the x direction such that fluid particles were allowed to recirculate, approximating an infinite domain (see Zhu et al [16]). For the case of Poiseuille flow, flow was driven from rest by a constantly applied body force of $F = 10^{-4} ms^{-2}$. For Couette flow, flow was driven by assigning the top solid boundary a constant velocity of $V_0 = 1.25 \times 10^{-5} ms^{-1}$. In both cases, a sound speed of $c = 5 \times 10^{-5} ms^{-1}$ was chosen and the simulation was continued until equilibrium was achieved.

Fig. 4 provides results for particle velocity for Poiseuille flow at a range of times compared to the analytical solution of the Navier-Stokes equations. This analytical solution was determined from the expression provided by Morris et al [26], i.e.

$$v_x(y,t) = \frac{F}{2\nu} y(y-L) + \sum_{n=0}^{\infty} \frac{4FL^2}{\nu\pi^3 (2n+1)^3} \sin\left(\frac{\pi y}{L}(2n+1)\right) \exp\left(-\frac{(2n+1)^2 \pi^2 \nu}{L^2} t\right) \quad (24)$$

where L is the width of the channel and $v_x(y,t)$ is the fluid velocity calculated at position y and time t. Comparable to the results observed by Morris et al, the determined SPH results deviated from the exact solution by no more than 0.59%. As with Morris's findings, this figure was observed to degrade with increasing mesh coarseness due, primarily, to a loss of resolution at the boundary surface.

Fig. 5 provides velocity profile results from the Couette flow simulations. Again from Morris

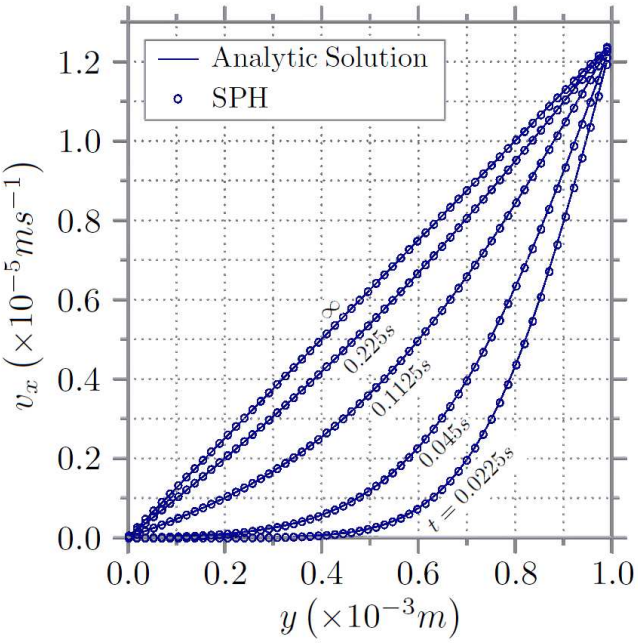

Figure 5. Results for fluid velocity for Couette flow comparing SPH simulation results with the analytical solution.

et al [26], the analytical solution used for comparison was determined from

$$v_x(y,t) = \frac{V_0}{L}y + \sum_{n=0}^{\infty} \frac{2V_0}{n\pi}(-1)^n \sin\left(\frac{n\pi}{L}y\right) \exp\left(-\nu\frac{n^2\pi^2}{L^2}t\right) \tag{25}$$

Again, high accuracy was observed with SPH results less than 0.2% from that of the analytical solution.

A study of the stability of the solution at long time was carried out for the case of Couette flow. Fig. 6 shows initial and long time particle configurations for a section of the problem. In the absence of flow obstructions, particles remained relatively ordered for the entire span of the test. The long time flow rate is provided in Fig. 7 showing that equilibrium was reached after approximately 1 sec, and remained relatively stable for the remainder of the test.

The accuracy of the results presented here validate the developed no-slip boundary method in the presence of straight boundaries. The remainder of this section addresses the more complex case of non-straight boundaries.

3.2. Two-Dimensional Flow Through a Square Array of Cylinders

A well defined example of two-dimensional flow is that of flow past a periodic array of infinite cylinders. Such models have been used extensively as ideal two-dimensional porous media for testing of various numerical methods including SPH [26, 16, 40, 41, 42, 8, 43, 44]. We limit our focus to the case of a square array of cylinders following the work of Zhu et al [16] (see Fig. 8).

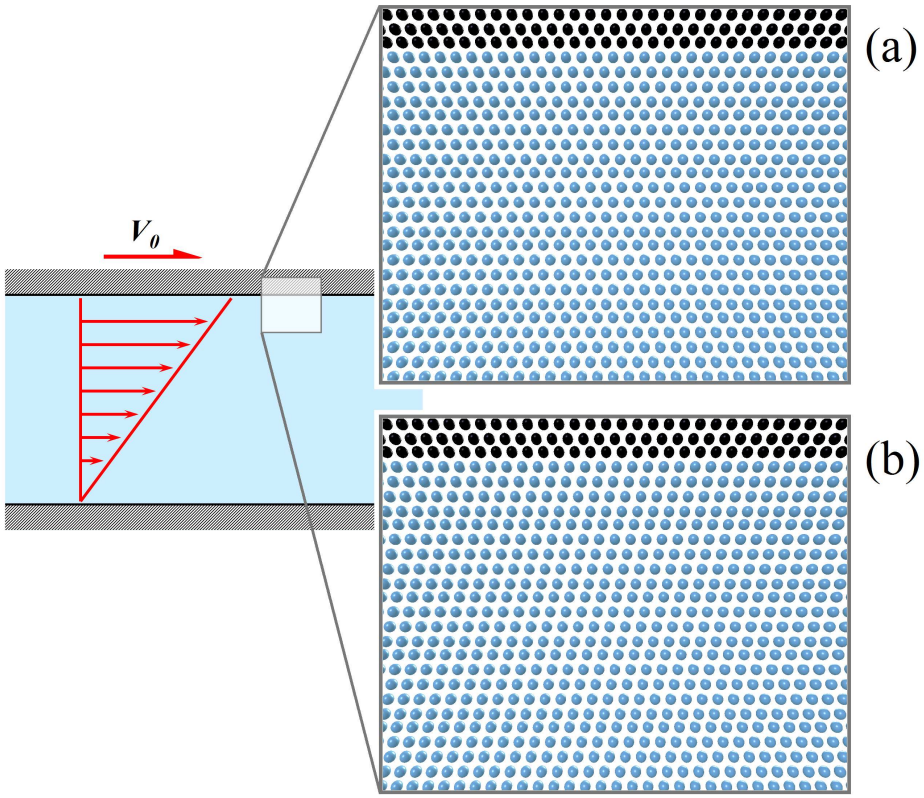

Figure 6. Model geometry for Couette flow simulation showing particle distribution at (a) initial configuration time = 0 sec, and (b) time step 2,660,000, time = 26.6 sec.

Due to symmetry, a model of such an array of cylinders can be reduced to the two-dimensional unit cell shown in the right of Fig. 8. As for the one-dimensional case above, recirculating periodic boundaries [16], here in the x and y directions, allowed the unit cell to approximate an infinite domain. For all simulations, a center-to-center cylinder distance, d, of $1 \times 10^{-3}m$ was chosen and the fluid was assigned the properties of water ($\rho_0 = 10^3 kgm^{-3}$, $\nu = 10^{-6}m^2s^{-1}$).

Investigated during the simulations was the effect of *solid volume fraction*, ϕ, on fluid flow, where

$$\phi = \frac{V_{solid}}{V_{cell}} \tag{26}$$

and where V_{solid} is the volume of a solid cylinder, while V_{cell} is the total volume of the unit cell. This is conjugate to *porosity*, n, where $n = (1 - \phi)$. Simulations for various cylinder radii, r, were carried out corresponding to solid volume fractions of ϕ = 0.05, 0.1, 0.2, 0.3, 0.4, 0.5, 0.6 and 0.7 (i.e. r = 0.126, 0.178, 0.252, 0.309, 0.357, 0.399, 0.437 and $0.472mm$). In all simulations, flow was driven from rest to equilibrium by a constant body force $F = 0.049ms^{-2}$ and an artificial sound speed of $c = 0.045ms^{-1}$ was chosen.

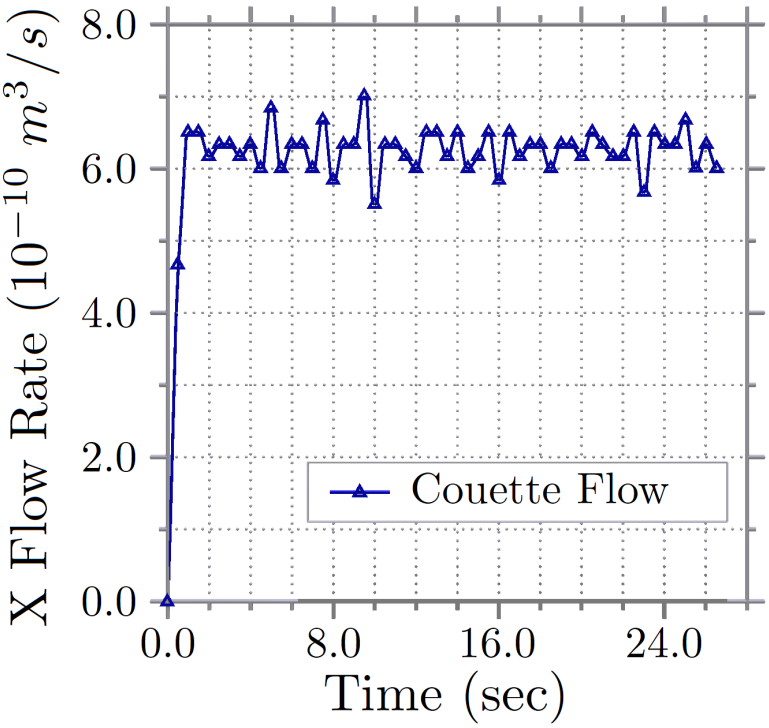

Figure 7. Long time response of flow rate for Couette flow.

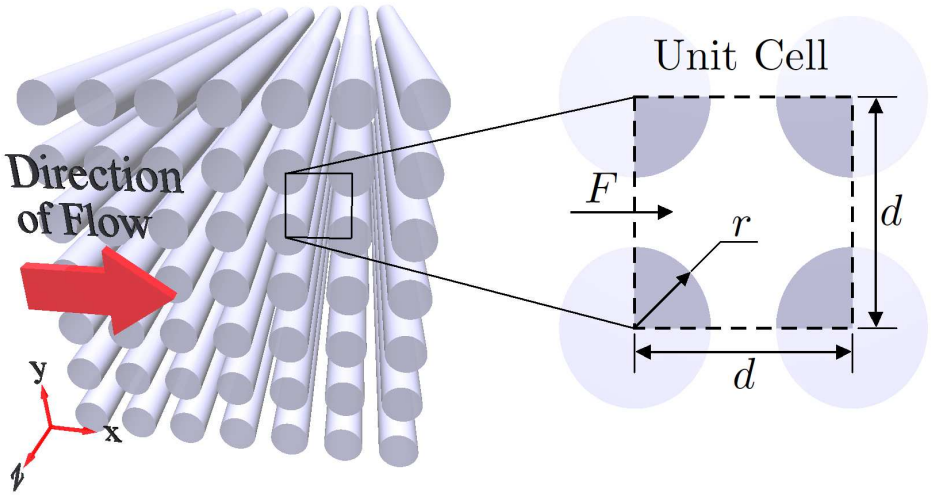

Figure 8. Square periodic array of infinite cylinders.

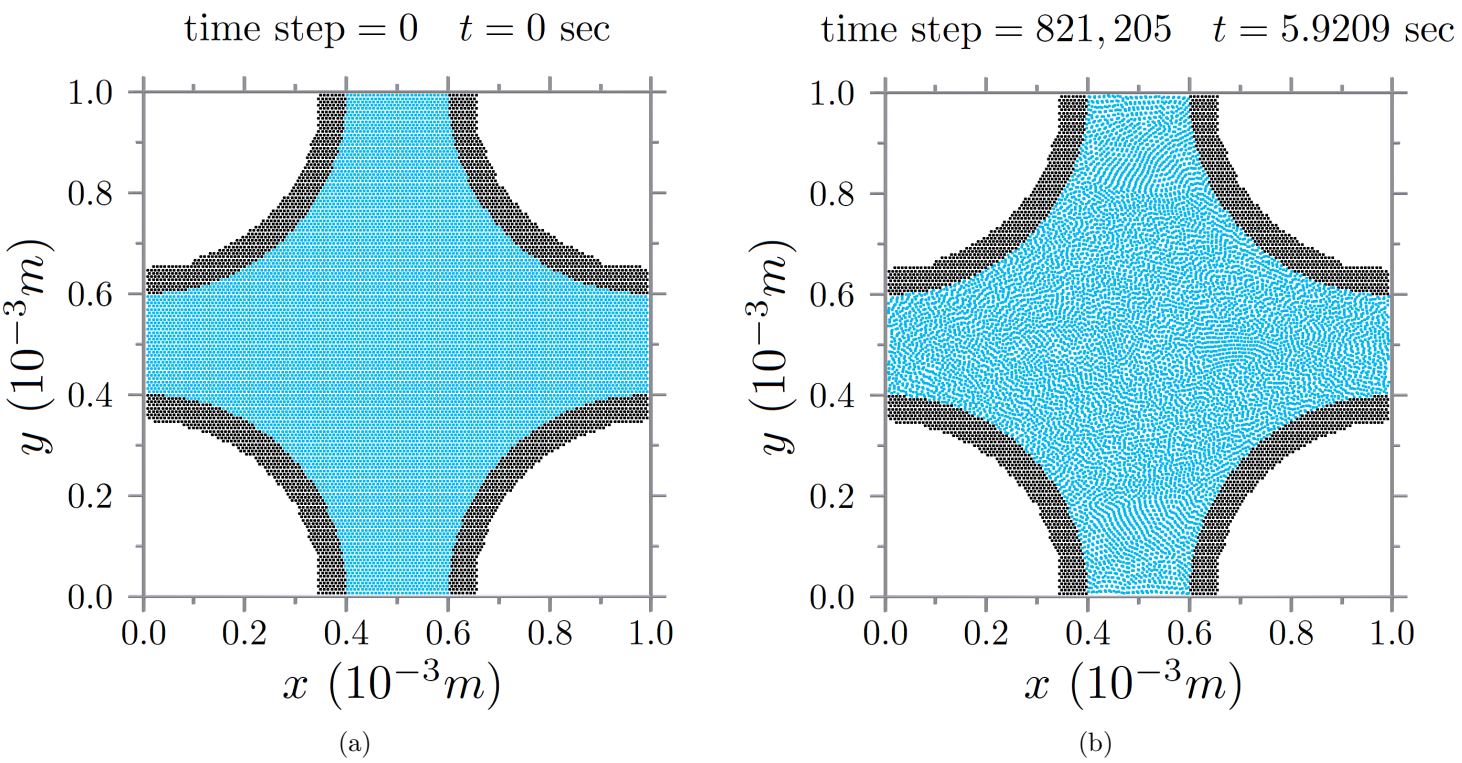

Figure 9. (color online). Particle positions for square array of cylinders ($\phi = 0.5$) at (a) ordered initial configuration, and (b) fully disordered long time configuration. Boundary particles are shown in black and fluid particles in blue.

Particles were initially arranged on a uniform two-dimensional hexagonal grid and those positioned within the bounds of the solid cylindrical grains were specified as boundary particles as described in Section 2.2. Boundary particles located further than $6h$ from a boundary surface contributed nothing to the solution and so were deleted for efficiency. Diagrams of initial and 'late time' particle distributions are provided in Fig. 9 (a) and (b) respectively.

3.2.1. Characterization of Flow

Consistent with most other works on fluid flow in porous media, in this paper we characterize flow in terms of a *friction coefficient*, K, and the *permeability*, k [4].

The friction coefficient is an indication of the resistance of a porous media to flow and is typically given as a dimensionless form of the drag force, F_d [45]. For the case of a cylinder of infinite length in an infinitely dilute domain (i.e. $\phi \to 0$), Huner and Hussey [46] define cylinder drag per unit length as $F_d = 4\pi\mu U\epsilon$ where U is the superficial fluid velocity and ϵ is a term based on the Reynolds number of the flow. Hasimoto [1] and Sangani and Acrivos [3] use similar terms for cylinder drag. Neglecting the dimensionless ϵ, an appropriate expression

for friction coefficient then takes the form

$$K = \frac{F_d}{4\pi\mu U} \tag{27}$$

where the drag force, F_d, is determined directly during flow simulations as the net force exerted by fluid particles on the lattice of cylinders. Additionally, the volumetric flow rate, q, can be determined during simulation as the sum of fluid particle volumes (i.e. $\sum V_i = \sum m_i/\rho_i = \sum 1/n_i$) traveling out the model bounds over time. From this, fluid velocity, u, is calculated as $u = q/A$, where A is the cross-sectional area of the unit cell, and the superficial fluid velocity is then determined from $U = (1 - \phi)\, u$ [45].

Determination of the permeability, k, of a porous media develops directly from Darcy's law, i.e.

$$\mu U = -k\nabla\bar{p} \tag{28}$$

where $\nabla\bar{p}$ is the mean pressure gradient driving flow. Following Larson and Higdon [4], the mean pressure gradient is directly related to the drag force on the cylindrical inclusions via $\nabla\bar{p} = -F_d/V_{cell}$, so that from (27) and (28), the permeability can be expressed

$$k = \frac{V_{cell}}{4\pi K} \tag{29}$$

Nondimensionalizing this term with respect to d^2, dimensionless permeability is then given

$$\frac{k}{d^2} = \frac{1}{K}\left(\frac{V_{cell}}{4\pi d^2}\right) \tag{30}$$

3.2.2. Mesh Sensitivity

Particle number for each model geometry was chosen to provide sufficient resolution whilst minimizing computational effort. Minimum particle density is typically limited by the narrowest model region. As a consequence, models with the narrowest pore throats require the greatest number of particles to achieve a sufficiently accurate results for flow. Zhu et al [16] suggests that a minimum of 15 fluid particles should span the narrowest model dimension in two-dimensional flow problems. In our experience we have found this figure to correspond to results within approximately 5% of the best case asymptotic solution, i.e. the value approached when progressively increasing particle number to infinity. In the results presented in the following section, we have favored the use of particle densities corresponding to approximately 25 fluid particles spanning the model pore throats, having observed this figure to improve accuracy to within 1% of the ideal.

3.2.3. Flow Results

Simulation results for friction coefficient at the various solid volume fractions are provided in Table I. These results are compared to those published by Zhu et al [16] using a similar SPH simulator and those of Sangani and Acrivos [40] using an algebraic numerical method. These results are also plotted in Fig. 10. It is evident that the present results agree well with the widely accepted results of Sangani and Acrivos. While the present results represent an improvement over those of Zhu et al, this can mainly be attributed to the increased particle density. Tests carried out with comparable particle numbers resulted in a similar order of accuracy. Corresponding results for dimensionless permeability are plotted in Fig. 11.

Table I. Friction coefficient, K, for various values of solid volume fraction, ϕ, for flow through a square array of cylinders. Results determined in the current work are compared to several previously published results for the same problem.

Solid Volume Fraction (ϕ)	K		
	Present Results	Zhu et al [16]	Sangani and Acrivos [40]
0.05	1.25	-	1.24
0.1	2.00	-	1.98
0.2	4.12	-	4.10
0.3	8.24	-	8.19
0.4	17.25	17.02	17.34
0.5	41.94	43.58	42.38
0.6	140.48	142.10	140.30
0.7	1066.83	1123.13	1075.89

Fig. 12 shows the long time response of flow rate for the case of a cylinder array with $\phi = 0.5$. Clearly, the flow very quickly reaches equilibrium state (after approximately 0.15 sec) and maintains this value well past the point at which particles become fully disordered (see Fig. 9 (b)). The results show the model and developed no-slip boundary method to be stable for long time porous media simulations.

3.3. Three-Dimensional Flow Through a Cubic Array of Consolidated Spheres

Ordered sphere packings have been used extensively within the literature as idealized three-dimensional porous media. Authors such as Hasimoto [1], Zick and Homsy [2] and Sangani and Acrivos [3] have each presented well verified results for flows through simple cubic, body- and face-centered cubic arrays of spheres with porosities ranging up to the close touching limits of the spheres. Unlike in the case of cylinders (Section 3.2), fluid flow will continue in sphere packs well past the point where sphere radii exceed the close touching limit (Fig. 13). Authors such as Larson and Higdon [4] and Roberts and Schwartz [47] have used such model geometries to represent consolidated porous media. In this work, we have tested the performance of the developed SPH code for three-dimensional flow using a simple cubic array of spheres with sphere radii up to, and past, the sphere close touching limits as per Larson and Higdon [4], see Fig. 13.

Again, symmetry of the periodic system facilitated the reduction of the model to the representative three-dimensional unit cell shown in the right of Fig. 13. Recirculating periodic boundaries were enforced in all three model dimensions and a center-to-center sphere distance, d, of $1 \times 10^{-3}m$ was chosen. The fluid was again assigned the properties of water ($\rho_0 = 10^3 kgm^{-3}$, $\nu = 10^{-6}m^2s^{-1}$).

For the sphere pack case, solid volume fraction is still given by equation (26) where now

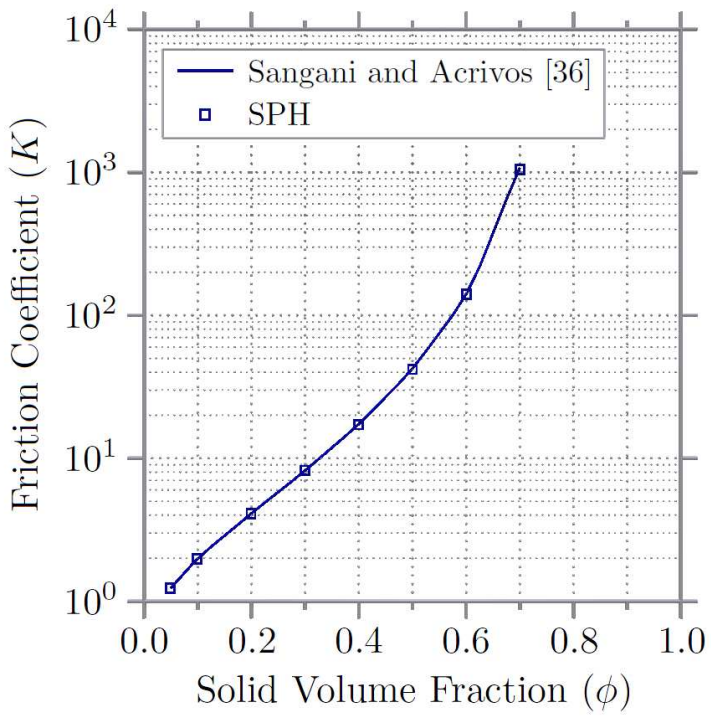

Figure 10. Friction coefficient.

V_{solid} corresponds to the volume of a spherical grain¶. A variety of solid volume fractions were used in the simulations following the work of Larson and Higdon [4]. These are listed later in Table II. In all simulations, flow was driven from rest by a constant body force of $F = 0.049ms^{-2}$ and an artificial sound speed of $c = 0.07ms^{-1}$ was chosen.

During model definition, SPH particles were initially arranged on a uniform three-dimensional hexagonal close packed grid and, as was the case for the cylindrical lattice of Section 3.2, particles positioned inside the bounds of solid spherical grains were designated as being boundary particles. Again, boundary particles greater than $6h$ from a boundary surface were removed.

3.3.1. Characterization of Flow

Like for the two-dimensional flow of Section 3.2, flow through the cubic array of consolidated spheres has been characterized in terms of a friction coefficient, K, and the permeability, k.

¶Note that the determination of this volume is arbitrary for sphere radii up to the close touching limit of the spheres and slightly more complex when spheres overlap.

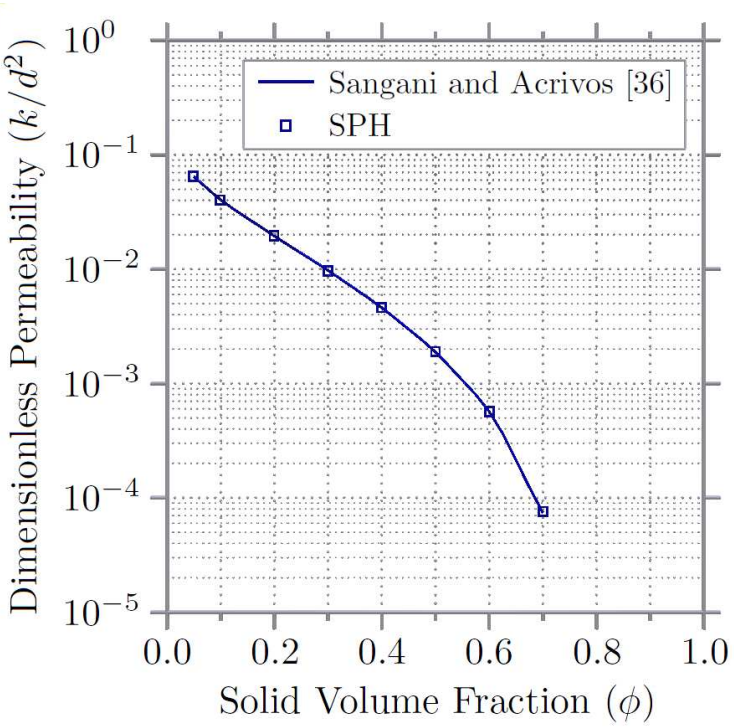

Figure 11. Dimensionless permeability.

For the case of a spherical grain in infinite dilution, the drag force, F_d, can be expressed via the Stokes-Einstein form, $F_d = 6\pi\mu rU$ [45]. Using this term to nondimensionalize the sphere pack drag, we establish the friction coefficient used by authors such as Zick and Homsy [2] and Larson and Higdon [4] as

$$K = \frac{F_d}{6\pi\mu rU} \tag{31}$$

The force and velocity terms in (31) were determined from simulation results in the same way as has been described earlier in Section 3.2.1.

Once again, permeability was determined through Darcy's law with the dimensionless form being given by

$$\frac{k}{d^2} = \frac{1}{K}\left(\frac{V_{cell}}{6\pi r d^2}\right) \tag{32}$$

3.3.2. Mesh Sensitivity

While the relationship between SPH solution accuracy and particle density in the presence of narrow flow channels is fairly well defined in two-dimensions (see [16]), the same cannot be said of three-dimensions. The lack of published work on three-dimensional SPH flow simulations has meant little work has been done on the subject. The problem is compounded by the significant

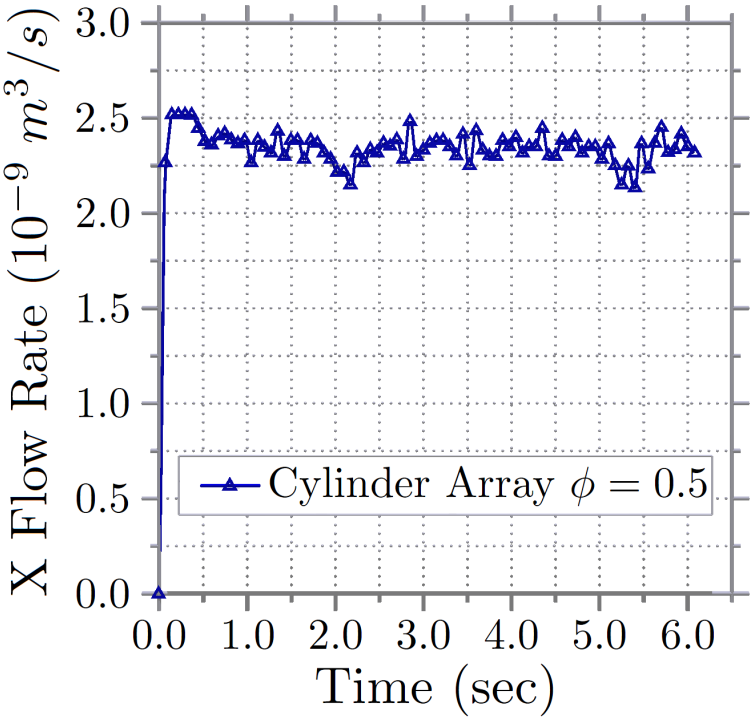

Figure 12. Long time response of flow rate for a square array of cylinders with $\phi = 0.5$.

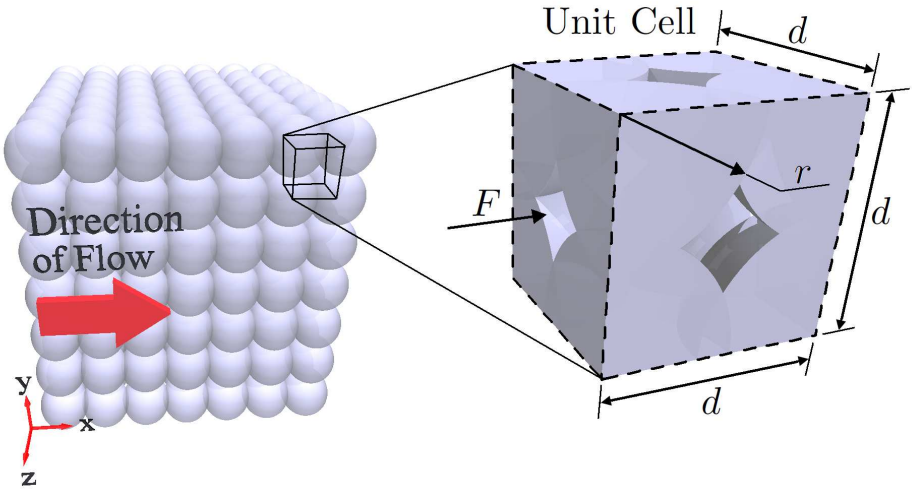

Figure 13. Cubic arrangement of consolidated spheres.

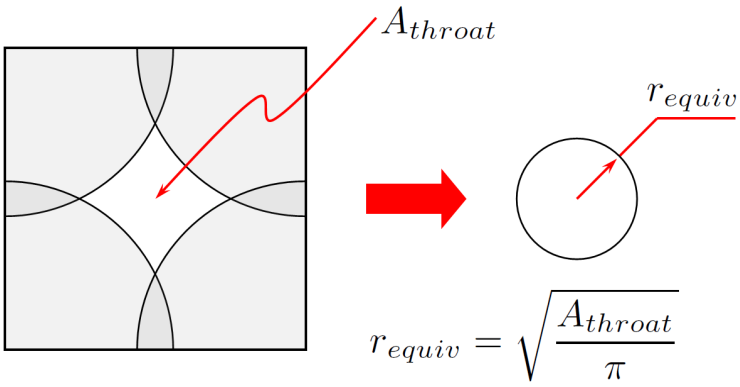

Figure 14. Determination of an equivalent circular throat area for mesh density specification.

increase in pore throat complexity when moving from two- to three-dimensions for even the most simple of model geometries; clearly it is more challenging to determine a characteristic pore throat dimension when considering the sphere packing of Fig. 13 compared to the two-dimensional case of Fig. 8. With the pore throats being the critical limitation on mesh density, a benchmark for choosing mesh size would be highly desirable.

Throughout simulation runs (see the next section for the full results set), a certain amount of trial and error has provided insight into the relationship between mesh density and result accuracy. We have found it effective to characterize each pore throat via a circle of equivalent throat area, see Fig. 14. Particle density should then be defined such that approximately 30 fluid particles span the proxy circular throat, i.e.

$$h \simeq \frac{2}{30}\sqrt{\frac{A_{throat}}{\pi}} \tag{33}$$

This technique produces results within approximately 2% of the ideal asymptotic result for an infinitely dense model. Additionally, this methodology is applicable for a wide range of pore throat geometries of arbitrary complexity. More detailed verification of such a method is required, however, within the context of the current investigation, the proposed method has proven to be effective.

3.3.3. Flow Results

The full set of simulation results for friction coefficient at the various solid volume fractions are provided in Table II. The results are contrast to those of Larson and Higdon [4] demonstrating excellent agreement at all ranges of porosity. Friction coefficient results are plotted in Fig. 15, while results for dimensionless permeability are plotted in Fig. 16.

Table II. Friction coefficient, K, for various values of solid volume fraction, ϕ, for flow through a cubic array of consolidated spheres. Results determined in the current work are compared to previously results from Larson and Higdon [4] for the same problem.

Solid Volume Fraction (ϕ)	K	
	Present Results	Larson and Higdon [4]
0.001	1.210	1.212
0.008	1.538	1.5247
0.027	1.946	2.0077
0.064	2.777	2.8102
0.125	4.253	4.292
0.216	7.449	7.4423
0.343	15.61	15.402
0.450	27.92	28.09
0.5236	41.95	41.99
0.53	43.78	43.6
0.55	47.93	48.8
0.60	66.41	66.10
0.65	93.29	93.36
0.70	137.37	139.8
0.75	233.48	228.3
0.80	423.10	426.9
0.85	1.003×10^3	1.020×10^3
0.90	4.366×10^3	4.290×10^3

4. CONCLUSIONS

A new approach to addressing no-slip boundary conditions in SPH simulations of low Reynolds number flows has been presented. The method provides a versatile and numerically efficient way of enforcing such boundary conditions for a wide range of problems. Results from grain scale fluid flow simulations for two- and three-dimensional porous media have demonstrated excellent agreement with those from a variety of well verified numerical and analytical solutions from the literature. Of particular significance are the results for flow through consolidated three-dimensional porous media with porosities ranging down to levels indicative of actual permeable rock (i.e. $n = 10\%$). To our knowledge, this is the first time SPH has been applied to this problem.

While the verification of SPH as an accurate analysis tool for single-phase flows is a non-trivial result, the true benefits of such a result are realized when applying SPH to problems involving multi-phase flows and complex pore geometries. Particularly, the ability of SPH to simulate multiple fluid phases with accurate expression of surface tension and interfacial properties such as wettability and contact angle (see [30, 18, 48]), make the method an extremely powerful numerical tool. By verifying the explicit accuracy of the method to simulate

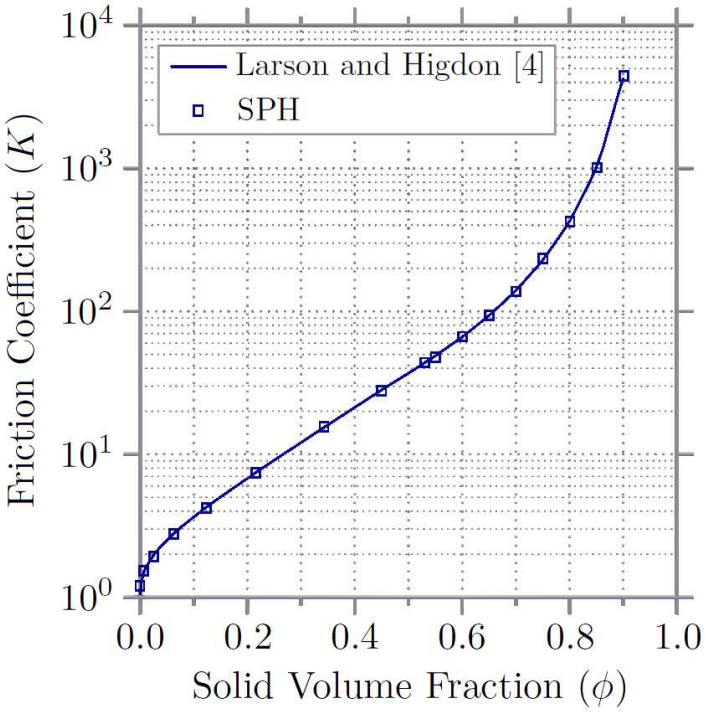

Figure 15. Friction coefficient.

flow, the power of these capabilities become all the more significant. A major advantage of the no-slip boundary method presented in this work is the ease with which it can be extended to account for multiple fluid phases including surface tension.

ACKNOWLEDGEMENTS

The authors would like to acknowledge the Schlumberger Doll Research Center and Saudi Aramco for their joint financial support of this research.

REFERENCES

1. Hasimoto H. On the periodic fundamental solutions of the Stokes equations and their application

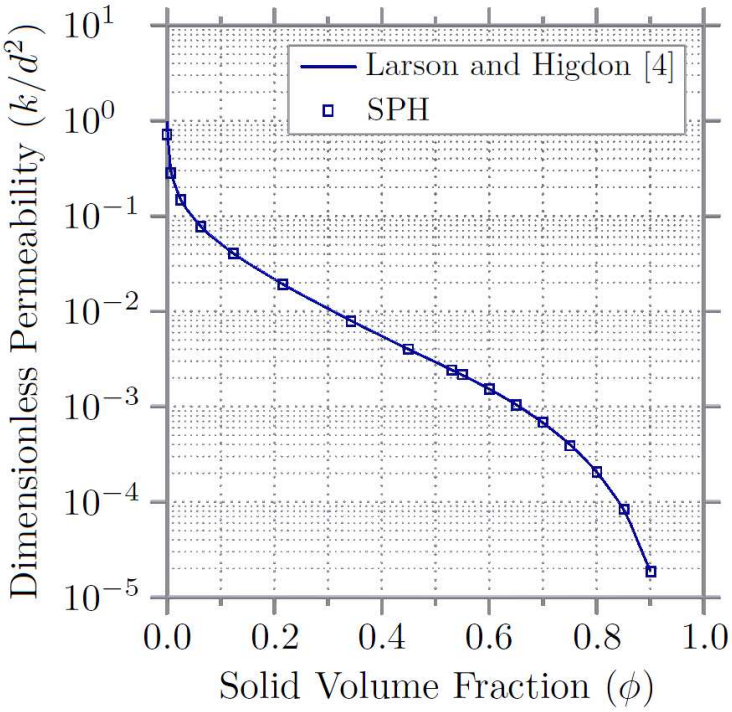

Figure 16. Dimensionless permeability.

to viscous flow past a cubic array of spheres. *Journal of Fluid Mechanics* 1959; **5**(2):317–328, doi: 10.1017/S0022112059000222.

2. Zick AA, Homsy GM. Stokes flow through periodic arrays of spheres. *Journal of Fluid Mechanics* 1982; **115**:13–26, doi:10.1017/S0022112082000627.
3. Sangani AS, Acrivos A. Slow flow through a periodic arrays of spheres. *International Journal of Multiphase Flow* 1982; **8**(4):343–360, doi:10.1016/0301-9322(82)90047-7.
4. Larson RE, Higdon JJL. A periodic grain consolidation model of porous media. *Physics of Fluids A* 1989; **1**(1):38–46, doi:10.1063/1.857545.
5. Narasimhan TN, Witherspoon PA. An integrated finite difference method for analyzing fluid flow in porous media. *Water Resources Research* 1976; **12**(1):57–64, doi:10.1029/WR012i001p00057.
6. Russell TF, Wheeler MF. Finite element and finite difference methods for continuous flows in porous media. *Mathematics of Reservoir Simulation*, Ewing RE (ed.), SIAM: Philadelphia, PA, 1983; 35–106.

7. Schwartz LM, Martys N, Bentz DP, Garboczi EJ, Torquato S. Cross-property relations and permeability estimation in model porous media. *Physical Review E* 1993; **48**(6):4584–4591, doi:10.1103/PhysRevE.48.4584.
8. Meegoda NJ, King IP, Arulanandan K. An expression for the permeability of anisotropic granular media. *International Journal for Numerical and Analytical Methods in Geomechanics* 1989; **13**(6):575–598, doi:10.1002/nag.1610130602.
9. Cancelliere A, Chang C, Foti E, Rothman DH, Succi S. The permeability of a random medium: Comparison of simulation with theory. *Physics of Fluids A: Fluid Dynamics* 1990; **2**(12):2085–2088, doi:10.1063/1.857793.
10. Huang H, Meakin P, Liu MB. Computer simulation of two-phase immiscible fluid motion in unsaturated complex fractures using a volume of fluid method. *Water Resources Research* 2005; **41**:W12 413, doi:10.1029/2005WR004204.
11. Li XY, Huang H, Meakin P. Level set simulation of coupled advection-diffusion and pore structure evolution due to mineral precipitation in porous media. *Water Resources Research* 2008; **44**:W12 407, doi:10.1029/2007WR006742.
12. Lucy LB. A numerical approach to the testing of the fission hypothesis. *Astronomical Journal* 1977; **82**:1013–1024, doi:10.1086/112164.
13. Gingold RA, Monaghan JJ. Smoothed particle hydrodynamics: Theory and application to non-spherical stars. *Monthly Notices of the Royal Astronomical Society* 1977; **181**:375–389.
14. Monaghan JJ. Smoothed particle hydrodynamics. *Annual Review of Astronomy and Astrophysics* 1992; **30**:543–574, doi:10.1146/annurev.aa.30.090192.002551.
15. Monaghan JJ. Simulating free surface flows with SPH. *Journal of Computational Physics* 1994; **110**:399–406, doi:10.1006/jcph.1994.1034.
16. Zhu Y, Fox PJ, Morris JP. A pore-scale numerical model for flow through porous media. *International Journal for Numerical and Analytical Methods in Geomechanics* 1999; **23**:881–904, doi:10.1002/(SICI)1096-9853(19990810)23:9{\%3C}881::AID-NAG996{\%3E}3.0.CO;2-K.
17. Monaghan JJ. Smoothed particle hydrodynamics. *Reports on Progress in Physics* 2005; **68**:1703–1759, doi:10.1088/0034-4885/68/8/R01.
18. Tartakovsky AM, Meakin P. Pore scale modeling of immiscible and miscible fluid flows using smoothed particle hydrodynamics. *Advances in Water Resources* 2006; **29**:1464–1478, doi:10.1016/j.advwatres.2005.11.014.

19. Liu GR, Liu MB. *Smoothed Particle Hydrodynamics: a meshfree particle method*. World Scientific: Singapore, 2007.

20. Bui HH, Fukagawa R, Sako K, Ohno S. Lagrangian meshfree particles method (SPH) for large deformation and failure flows of geomaterial using elastic-plastic soil constitutive model. *International Journal for Numerical and Analytical Methods in Geomechanics* 2008; **32**(12):1537–1570, doi:10.1002/nag.688.

21. Randles PW, Libersky LD. Smoothed particle hydrodynamics: Some recent improvements and applications. *Computer Methods in Applied Mechanics and Engineering* 1996; **139**:375–408, doi:10.1016/S0045-7825(96)01090-0.

22. Liu M, Meakin P, Huang H. Dissipative particle dynamics simulation of pore-scale multiphase fluid flow. *Water Resources Research* 2007; **43**:W04 411, doi:10.1029/2006WR004856.

23. Liu M, Meakin P, Huang H. Dissipative particle dynamics simulations of multiphase fluid flow in microchannels and microchannel networks. *Physics of Fluids* 2007; **19**:033 302, doi:10.1063/1.2717182.

24. Holmes DW, Williams JR, Tilke P. An events based algorithm for distributing concurrent tasks on multi-core architectures. *Computer Physics Communications* 2010; **181**(2):341–354, doi:10.1016/j.cpc.2009.10.009.

25. Takeda H, Miyama SM, Sekiya M. Numerical simulation of viscous flow by smoothed particle hydrodynamics. *Progress of Theoretical Physics* 1994; **92**(5):939–960, doi:10.1143/PTP.92.939.

26. Morris JP, Fox PJ, Zhu Y. Modeling low Reynolds number incompressible flows using SPH. *Journal of Computational Physics* 1997; **136**:214–226, doi:10.1006/jcph.1997.5776.

27. Sigalotti LDG, Klapp J, Sira E, Meleán Y, Hasmy A. SPH simulations of time-dependent Poiseuille flow at low Reynolds numbers. *Journal of Computational Physics* 2003; **191**:622–638, doi:10.1016/S0021-9991(03)00343-7.

28. Zhu Y, Fox PJ. Smoothed particle hydrodynamics model for diffusion through porous media. *Transport in Porous Media* 2001; **43**:441–471, doi:10.1023/A:1010769915901.

29. Benz W. Smooth particle pydrodynamics - a review. *Numerical Modelling of Nonlinear Stellar Pulsations Problems and Prospects*, Buchler JR (ed.), 1990; 269–288.

30. Tartakovsky AM, Meakin P. A smoothed particle hydrodynamics model for miscible flow in three-dimensional fractures and the two-dimensional rayleigh-taylor instability. *Journal of Computational Physics* 2005; **207**:610–624, doi:10.1016/j.jcp.2005.02.001.

31. Hu XY, Adams NA. A multi-phase SPH method for macroscopic and mesoscopic flows. *Journal of Computational Physics* 2006; **213**:844–861, doi:10.1016/j.jcp.2005.09.001.

32. Hoover WG. Isomorphism linking smooth particles and embedded atoms. *Physica A* 1998; **260**:244–254, doi:10.1016/S0378-4371(98)00357-4.

33. Morris JP, Zhu Y, Fox PJ. Parallel simulations of pore-scale flow through porous media. *Computers and Geotechnics* 1999; **25**:227–246, doi:10.1016/S0266-352X(99)00026-9.

34. Morris JP. Simulating surface tension with smoothed particle hydrodynamics. *International Journal for Numerical Methods in Fluids* 2000; **33**:333–353, doi:10.1002/1097-0363(20000615)33:3{\%3C}333::AID-FLD11{\%3E}3.0.CO;2-7.

35. Herrnstein A, Wickett M, Rodrigue G. Structured adaptive mesh refinement using leapfrog time integration on a staggered grid for ocean models. *Ocean Modelling* 2005; **9**:283–304, doi:10.1016/j.ocemod.2004.07.002.

36. Tartakovsky AM, Meakin P, Scheibe TD, West RME. Simulations of reactive transport and precipitation with smoothed particle hydrodynamics. *Journal of Computational Physics* 2007; **222**:654–672, doi:10.1016/j.jcp.2006.08.013.

37. Morris JP. Analysis of smoothed particle hydrodynamics with applications. PhD Thesis, Monash University 1996.

38. Libersky LD, Petschek AG, Carney TC, Hipp JR, Allahdadi RA. High strain Lagrangian hydrodynamics: A three-dimensional SPH code for dynamic material response. *Journal of Computational Physics* 1993; **109**(1):67–75, doi:10.1006/jcph.1993.1199.

39. Tartakovsky AM, Meakin P. Simulation of unsaturated flow in complex fractures using smoothed particle hydrodynamics. *Vandose Zone Journal* 2005; **4**:848–855, doi:10.2136/vzj2004.0178.

40. Sangani AS, Acrivos A. Slow flow past periodic arrays of cylinders with application to heat transfer. *International Journal of Multiphase Flow* 1982; **8**(3):193–206, doi:10.1016/0301-9322(82)90029-5.

41. Larson RE, Higdon JJL. Microscopic flow near the surface of two-dimensional porous media. Part 2. Transverse flow. *Journal of Fluid Mechanics* 1987; **178**:119–136, doi:10.1017/S0022112087001149.

42. Sangani AS, Yao C. Transport processes in random arrays of cylinders. II. Viscous flow. *Physics of Fluids* 1988; **31**(9):2435–2444, doi:10.1063/1.866596.

43. Edwards DA, Shapiro M, Bar-Yoseph P, Shapira M. The influence of reynolds number upon the apparent permeability of spatially periodic arrays of cylinders. *Physics of Fluids A: Fluid Dynamics* 45-55; **2**:1, doi:10.1063/1.857691.

44. Ghaddar CK. On the permeability of unidirectional fibrous media: A parallel computational approach. *Physics of Fluids* 1995; **7**(11):2563–2586, doi:10.1063/1.868706.

45. van der Hoef MA, Beetstra R, Kuipers JAM. Lattice-Boltzmann simulations of low-Reynolds-number flows

past mono- and bidisperse arrays of spheres: results for the permeability and drag force. *Journal of Fluid Mechanics* 2005; **528**:233–254, doi:10.1017/S0022112004003295.

46. Huner B, Hussey RG. Cylinder drag at low Reynolds number. *The Physics of Fluids* 1977; **20**(8):1211–1218, doi:10.1063/1.862001.
47. Roberts JN, Schwartz LM. Grain consolidation and electrical conductivity in porous media. *Physical Reveview B* 1985; **31**(9):5990–5997, doi:10.1103/PhysRevB.31.5990.
48. Tartakovsky AM, Meakin P. Modeling of surface tension and contact angles with smoothed particle hydrodynamics. *Physical Review E* 2005; **72**:1–9, doi:10.1103/PhysRevE.72.026301.